NANOSYSTEMS:
PHYSICS, CHEMISTRY, MATHEMATICS

Original article

Khramov A.S., et al. *Nanosystems: Phys. Chem. Math.*, 2025, **16** (6), 755–762.
http://nanojournal.ifmo.ru
DOI 10.17586/2220-8054-2025-16-6-755-762

Subwavelength LIPSS-based nanopatterning of thin titanium films

Andrey S. Khramov[a], Maksim D. Vasilev[b], Dmitry A. Sinev[c], Elena A. Shakhno[d]

ITMO University, St. Petersburg, Russia

[a]askhramov@itmo.ru, [b]mdvasilev@itmo.ru, [c]sinev@itmo.ru, [d]elena.shakhno@mail.ru

Corresponding author: Andrey S. Khramov, askhramov@itmo.ru

PACS 42.62.-b, 42.79.Dj, 42.82.Cr

ABSTRACT Precise nanopatterning of thin films is an important task in production of modern optoelectronics and photonics elements. Direct recording of laser-induced periodic surface structures (LIPSS) is a promising tool for direct subwavelength nanopatterning. Recent studies show that the dynamics of LIPSS formation changes significantly if the film is relatively thin. Here we present a comprehensive analytical model aiming to bridge the gap between the expected dynamics of electromagnetic fields during LIPSS formation and experimentally obtainable nanopatterning results. The phenomenological model of surface electromagnetic wave (SEW) propagation at the film–substrate interface illustrates the mechanism of LIPSS formation using a periodic distribution of SEW energy concentration. SEW features are calculated depending on metal film thickness, and positive feedback between the local thickness of the growing oxide layer and the SEW energy concentration is unveiled. Changes in LIPPS formation mechanisms are confirmed experimentally on titanium films with different thickness. These findings shed light on the intrinsic physical mechanisms of LIPSS formation on thin metal films and ease the possibilities for LIPPS applications for nanopatterning.

KEYWORDS laser-induced periodic surface structures, LIPSS, nanopatterning, thin films, direct laser writing

ACKNOWLEDGEMENTS Dmitry A. Sinev acknowledges the financial support of the Ministry of Science and Higher Education of the Russian Federation (No. FSER-2025–0007). Film deposition was conducted in the Interdisciplinary Resource Center for Nanotechnology of St. Petersburg State University within the framework of research project SPbSU: 125021702335-5. Andrey S. Khramov and Maksim D. Vasilev thank the ITMO University NIRMA project No 624128 for the support of students' research.

FOR CITATION Khramov A.S., Vasilev M.D., Sinev D.A., Shakhno E.A. Subwavelength LIPSS-based nanopatterning of thin titanium films. *Nanosystems: Phys. Chem. Math.*, 2025, **16** (6), 755–762.

1. Introduction

Nanopatterning of thin films is an important task in production of modern optoelectronics and photonics elements [1]. Thin transparent coatings textured to get the regular nanogrid or mesh are used to enhance substrate optical properties [2], regulate radiative cooling [3], or help with introducing the light into waveguide [4].

Controlled formation of laser-induced periodic surface structures (LIPSS) is a promising tool for direct subwavelength nanopatterning, with numerous applications in sensing [5, 6], tribology [7], cell growth management [8], and protective marking [9, 10]. LIPSS appear spontaneously on a wide range of the materials under a focused laser light as periodic reliefs much narrower than the beam width, with periods Λ of about laser wavelength λ or less. LIPSS appearance is usually linked with the emergence of surface electromagnetic wave (SEW) scattering alongside the air-material interface (which, as we will see later, is debatable in the case of LIPSS formation on thin films) [11]. SEW interference with initial laser light modulates the temperature field that gets imprinted into the material as an ablative or oxidative pattern [12]. Concise classification of LIPSS distincts high-spatial frequency LIPSS (with periods Λ of $\lambda/2$ and less) from low-spatial frequency LIPSS (LSFL, $\lambda/2 < \Lambda < \lambda$), with latter divided into LSFL-I (with grating vector $\vec{k}$ collinear with the orientation of linear polarization plane $\vec{E}$, typical for metal targets) and LSFL-II types ($\vec{k}$ oriented in perpendicular to the polarization, usual for the glasses and other non-metal substrates).

To the contrary of the expectations of LSFL-I formation on metal targets, some recent experimental studies [10,13–19] show that dynamics of LIPSS formation changes significantly when the film is relatively thin and its thickness reaches the value of 100 nm or less. Dostovalov et al. have shown in series of works [14, 17] the LIPSS formation with $\Lambda = 677$ – 700 nm both on 28 – 42 nm Cr and on 10 nm Hf films on BK7 glass substrates under the $\lambda = 1026$ nm laser light. Yang et al. [15] reported the LIPSS with $\Lambda = 320$ nm appearing on 20 nm Au films on ITO/glass substrates under the 532 nm laser irradiation. In [10], the usage of 1064 nm Yb-fiber laser source for producing the 1D and 2D LIPSS with $\Lambda = 720$ nm on 30 nm Ti films on quartz substrates was described in detail. Evidently, LIPSS period for thin films is dependent on the substrate refractive index, which indicates that when film is thin enough, the substrate plays a substantial role in distribution of the electromagnetic fields leading to LIPSS formation. There are few studies where

© Khramov A.S., Vasilev M.D., Sinev D.A., Shakhno E.A., 2025

experimental observations lead to the conclusions of the substrate influence [17, 20], and even less studies explaining this discrepancy [16, 21]. Here we present a comprehensive analytical model aiming to bridge the gap between the expected dynamics of electromagnetic fields during LIPSS formation and experimentally obtainable nanopatterning results.

2. Experimental results

2.1. Materials and methods

Samples of thin Ti films of different thicknesses on 1 mm thick quartz glass substrate were used for studying the critical film thickness for SEW formation on the film-substrate interface. Titanium films of 30, 60 and 80 nm thickness were produced by thermal sputtering in vacuum. An Yb-fiber laser with a central wavelength $\lambda = 1064$ nm, a pulse duration from 4 ns to 200 ns and a maximum output power 20 W was used to create LIPSS (MiniMarker-2 setup, Laser Center Ltd., St. Petersburg, Russia). A polarization control system was added to the optical path of the laser source: a Glan-Taylor prism isolated the linear component of polarization, and a half-wave plate was used to control the rotation of polarization. The laser spot size in the processing plane was $d = 55$ μm. An optical microscope Carl Zeiss Axio Imager A1.m (Carl Zeiss Microscopy GmbH, Munich, Germany) was used to visualize and assess LIPSS appearance. Period Λ_{exp} and regularity $\Delta\Lambda_{\text{exp}}$ were estimated by the two-dimensional fast Fourier transform method (2D-FFT) in the open source Gwyddion software. The modeling of SEW dynamics was performed using Wolfram Mathematica software.

2.2. Patterning results

Based on the results of the experiments, we have found that the LIPSS type changed from LSFL-II to LSFL-I for films thicker than 50 nm. As shown in Fig. 1(a), LIPSS on 30 nm film are formed in parallel to the polarization vector with a period of 720 ± 20 nm, closely corresponding to ratio of laser wavelength over the substrate's refractive index λ/n_{sub}, and can be classified as LSFL-II. Fig. 1 (b, c) shows the results of LIPSS formation on titanium films of 60 and 80 nm in thickness as a reference. As seen, in the center of the processed area, where the energy density is maximal, the disordered structures roughly with a period of 980 ± 150 nm ($\sim \lambda$) are formed, mostly in perpendicular to the polarization vector. At the same time, LIPSS of the LSFL-II type exist at the periphery of the scanning track, similar to the structures seen in Fig. 1(a). Processing regimes are as follows: the fluence is about 90 – 95 mJ/cm^2 for Fig. 1(a) and 360 – 450 mJ/cm^2 for Fig. 1(b–c), pulse repetition rates is 35 kHz for Fig. 1(a) and 70 kHz for Fig. 1(b–c). The discrepancy in the processing regimes is likely to be connected to the thermal stability of the films of different thicknesses, as the processing of 30 nm films with higher fluences have led to the ablation and peeling of the film. From these results, we can conclude that the thickness of 50 nm is not necessarily a threshold value, but rather the value for the detectable changes in the mechanisms of LIPSS formation, as the substrate's optical properties start to influence the process.

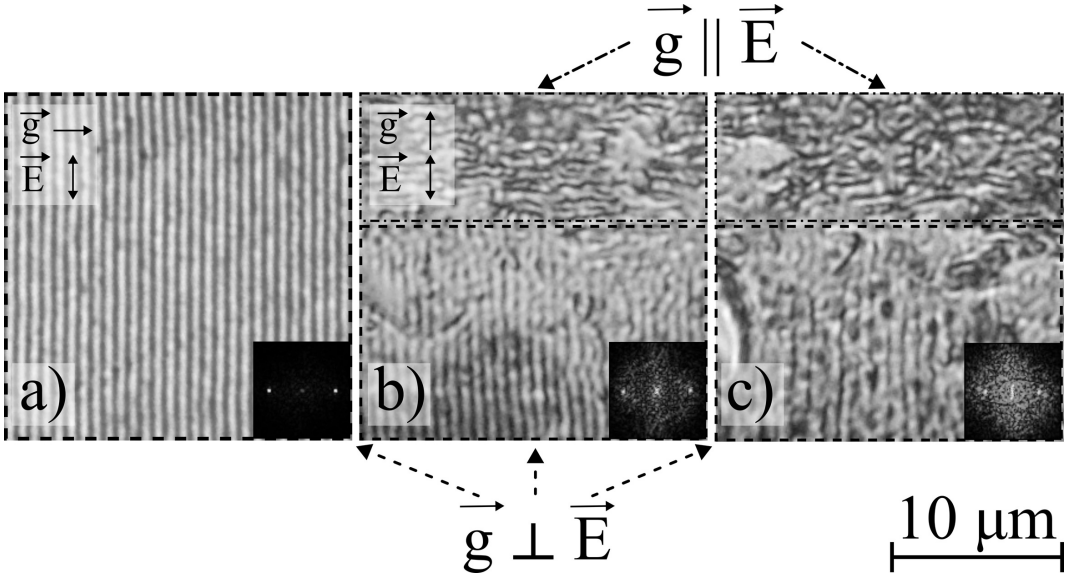

FIG. 1. Optical micrographs of LIPSS on Ti films with thicknesses of a) 30 nm, b) 60 nm, c) 80 nm. Regions with LSFL-II are highlighted by a dashed line, with LSFL-I by a dash-dot line. The central axis of the laser track coincides with the upper border of each image, scanning direction from left to right, polarization plane is oriented vertically. The scale bar is the same for all the images. Corresponding 2D-FFT spectra images are shown in the insets, borders of the spectra correspond to the spatial frequency of ± 0.5 μm^{-1}.

3. Discussion

3.1. Expected period estimations

The classical dispersion relation for an interface between two media gives the following condition for surface electromagnetic waves (SEWs) excitation at the air-film interface [22]:

$$\frac{\varepsilon_2'}{\varepsilon_1'} < -1, \quad \frac{\varepsilon_2''}{\varepsilon_2'} \ll 1, \tag{1}$$

where ε_i' is the real part and ε_i'' is the imaginary part of the dielectric permittivities ($i = 1, 2$). Index 1 corresponds to the air medium ($\varepsilon_1 = 1$) while index 2 refers to the metal film. For the titanium film $\varepsilon_2 = -4.0589 + 27.782i$ [23], so the condition (1) for the SEW formation is met. Therefore, we can calculate a SEW period Λ at the air-film interface by the following formula [22]:

$$\beta = \frac{\omega_L}{c}\sqrt{\frac{F_1 + F_2}{2}}, \quad \Lambda = \frac{2\pi}{\beta}, \tag{2}$$

where β is the SEW wavenumber, ω_L is the incident light angular frequency, c is the speed of light in vacuum, and F_1 and F_2 are the coefficients depending on ε_i' and ε_i'' that can be found by simple equations given in [22]. The dielectric permittivity ε_2 is taken constant since we consider the case of nanosecond laser irradiation with moderate intensities.

For laser wavelength $\lambda = 1064$ nm the classical model predicts LIPSS period to be 1062 nm. Thus, LIPSS formed as a result of laser radiation interference with SEWs at the air-film interface should have a period of about 0.998λ, which is common for bulk titanium. However, as shown in the Experimental section, the LIPSS period on optically thin titanium films was proven to be significantly lower and cannot be explained by SEWs generation at the air-film interface. Moreover, since the classical model regards SEW as a TM wave, it can only predict periods for LIPSS oriented perpendicular to the laser light polarization. Hence, it is reasonable to assume that LIPSS are formed as a result of SEWs generated at the film-substrate interface. Under this assumption we hereby present the model of LIPSS formation which explains the experimental results obtained on thin films.

3.2. Phenomenological model description

In the multi-pulse mode, at the first stage of exposure (at the first hundreds or thousands of pulses), there is presumably a rather large variety of SEWs formed on various inhomogeneities of the film surface and the film-substrate interface. Afterwards due to the competition of SEWs (positive feedback between the amplitude and period of the wave and local heating and oxidation of the film), a package of SEWs with similar characteristics is formed. As shown in experiments, LIPSS on optically thin metal films are formed with a period of $\Lambda = \lambda/n_{\text{sub}}$, which indicates that the structures are formed under the influence of SEWs generated on the surface of the substrate. This is the basis of our phenomenological model.

Each of the SEW packet waves can be represented as a surface wave formed when radiation acts at each point of the film surface, where the local thickness of the film and the local thickness of the oxide layer determine the local value of the intensity of radiation that has passed into the substrate. The main cause of the formation of LIPSS during thermochemical action on optically thin metal films is the unevenness of the absorption and transmission of the film due to a significant difference in the optical properties of the original metal film and the developing oxide, distributed in the film according to the period of the formed structures.

It is known that during the formation of SEW at the film-substrate interface under homogeneous conditions (in the absence of gradients of various parameters of the film and the substrate), the SEW is not absorbed in the film, but is distributed in the substrate as in a waveguide evenly across its thickness [24]. However, in our case of multi-pulse action at the stage of LIPSS formation, there is a dependence of the film transmittance along the coordinate, and the conditions for SEW formation become heterogeneous. This leads to a LIPSS formation with a period of $\Lambda = \lambda/n_{\text{sub}}$ in a thin metal film as a process based on a positive feedback between oxide thickness and SEW formation.

As film transmittance in the oxidized regions is higher than that in the non-oxidized regions, the amplitude of radiation penetrating into the substrate depends on the thickness of the oxide layer formed during the previous laser pulses (Fig. 2). We approximate the amplitude of the electric field vector that has passed into the substrate as follows:

$$E_t = E_{t0}(1 + B\cos(k_s x)), \tag{3}$$

where E_{t0} is its value at medium intensity (for simplicity, the intensity distribution in the laser spot is taken as constant), k_s is the wave vector of the SEW, the x-axis is directed along the film-substrate interface, B is the SEW modulation coefficient which depends on the ratio of the maximum and minimum laser intensities penetrating into the substrate (in the areas of the LIPSS, where the thickness of the oxide layer reaches the maximum and minimum values, respectively).

Thus, a TE-type SEW packet is generated at the film-substrate interface. The amplitude of each wave is proportional to the amplitude of the penetrating electromagnetic wave:

$$\vec{E_s} = \vec{E_{s0}}(1 + B\cos(k_s x))\exp(i(k_s x - \omega t) - \chi z), \tag{4}$$

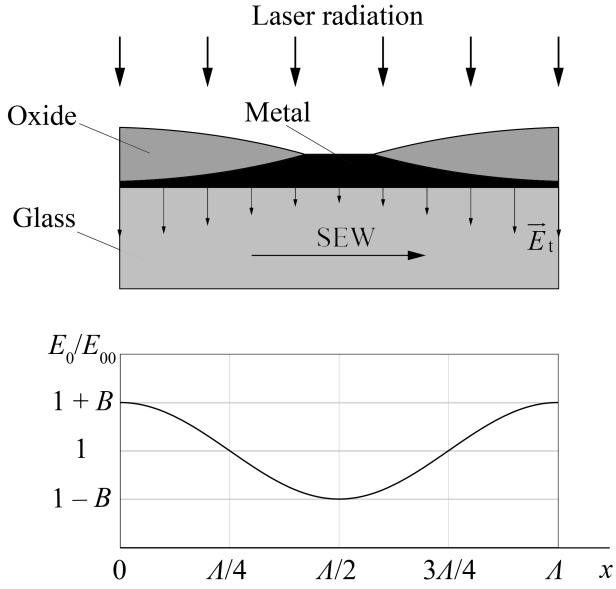

FIG. 2. Modulation of SEW by laser oxidation of the thin metal film

where $\vec{E}_{s0}$ is the vector of the amplitude of the SEW in the substrate at the average value of the transmitted wave intensity, the z-axis is directed into the substrate, ω is the frequency of the SEW, χ is the SEW attenuation parameter.

The main characteristic of the SEW that determines its ability to modulate the heating and oxidation of the film is value W proportional to its energy concentration:

$$W = \frac{1}{2}\varepsilon_0 n^2 |\vec{E}_s|^2. \tag{5}$$

To determine W, we substitute (4) into the wave equation $\nabla^2 \vec{E}_s - \frac{n^2}{c^2}\frac{\partial^2 \vec{E}_s}{\partial t^2} = 0$ which gives us the attenuation parameter of the SEW:

$$\chi = k_s \sqrt{\frac{2B\cos(k_s x)}{1 + B\cos(k_s x)}}. \tag{6}$$

As a special case for $B = 0$ (plane wave), we obtain the value $\chi = 0$ which, as expected, corresponds to a plane wave not modulated by film inhomogeneity, with $W = 0$.

The dependence of the relative energy concentration $W' = W/(\frac{1}{2}\varepsilon_0 n^2 |\vec{E_{s0}}|^2)$ on the coordinate along the wave vector for the time intervals of $t = \pi n/\omega$ $(n = 0, 1, 2, ...)$ obtained by formulas (4–6), is shown in Fig. 3. A significant increase in the concentration is observed near the points corresponding to the maximum thickness of the oxide $x = n\Lambda$.

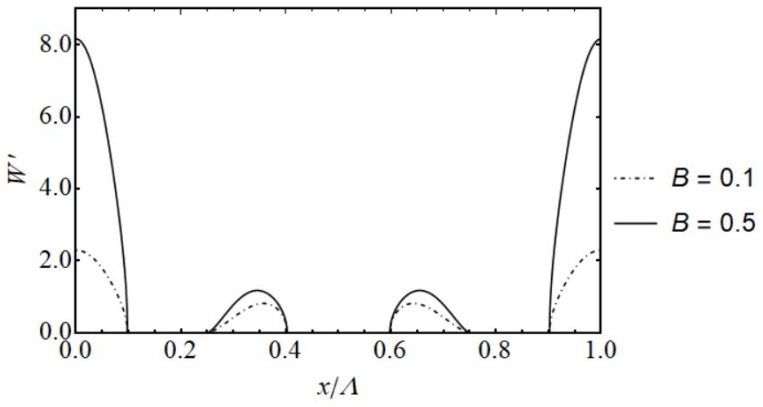

FIG. 3. Distribution of relative energy concentration W' along normalized coordinate for time values $\omega t = \pi n$

The change in the W' value over time at the point of maximum oxide thickness is shown in Fig. 4(a). The relative energy concentration oscillates in time, its change is described by the cosine square function, the oscillation period is π/ω. Since the oscillations are fast enough to have an effect on the film, the physical meaning lies in the average value of the relative energy concentration over time. It is equal to half of the maximum value $W'_{av} = \pi B^{1/2}(1+B)^{3/2}$. Thus, in the maxima of the oxide layer, with an increase in the parameter B (from pulse to pulse), the SEW relative energy concentration increases. Consequently, as the oxide thickness increases (when the film transmittance difference in the LIPSS maxima and minima increases), the effect on the film at the oxide layer maximum increases, which contributes to further oxide growth and positive opto-chemical feedback development. Full spatiotemporal dynamics of the relative energy concentration W' along the coordinate and in time for different stages of the LIPSS formation process is shown in Fig. 4(b–c).

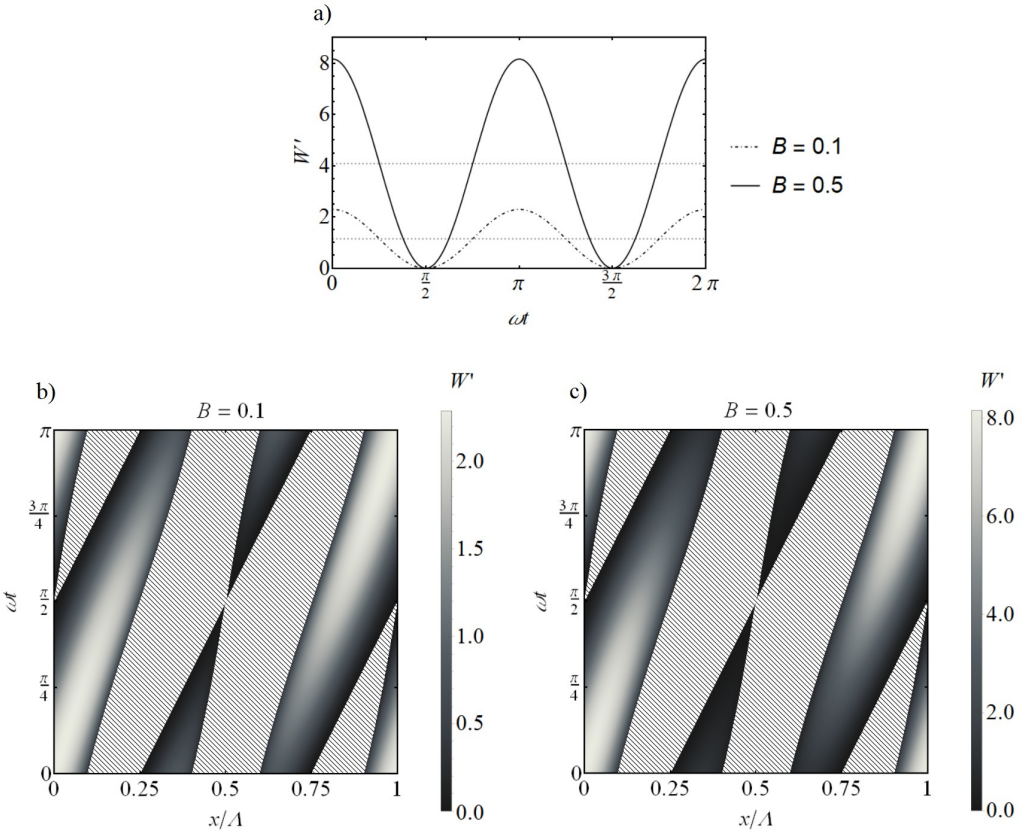

FIG. 4. (a) Dependence of the relative energy concentration W' at the point of maximal oxide layer thickness (for x/Λ equal to 0 or 1) on the time ωt for different values of the coefficient B. Dotted lines show the average values. Full spatiotemporal dynamics of W' on the coordinate x/Λ and time ωt at the early stage ($B = 0.1$) (b) and late stage ($B = 0.5$) (c) of LIPSS formation. Hatched are the areas where SEW propagates in the air.

An important characteristic of the LIPSS recording process is the thickness of the original film h. In particular, the maximum value of the modulation coefficient $B_{\max}$, which is achieved at complete (through) oxidation of the film at points $x = n\Lambda$, depends on it. The value of $B_{\max}$ determines the ratio G of the maximum $\Pi_{\max}$ and minimum $\Pi_{\min}$ film transmission at points $x = n\Lambda$ and $x = (n + 1/2)\Lambda$:

$$G = \frac{\Pi_{\max}}{\Pi_{\min}} = \frac{1 + B_{\max}}{1 - B_{\max}}. \tag{7}$$

Hence, $B_{\max} = (G-1)/(G+1)$. The value of the coefficient G is determined based on the optical properties of a metal film of a certain thickness and a completely oxidized film, taking into account the Pilling–Bedworth ratio. The thickness of the substrate layer $l = 1/\chi$, in which the SEW is distributed, and its relative value at $x = n\Lambda$ $L = l/\Lambda$, under conditions of a completely oxidized film at $x = n\Lambda$, i.e. $B = B_{\max}$, is determined from equation (6):

$$L = \frac{1}{2\pi}\sqrt{\frac{1 + B_{\max}}{2B_{\max}}}. \tag{8}$$

The calculated dependencies of the main characteristics of the final stage of the LIPSS formation process on the film thickness for titanium film on a quartz substrate [25] are shown in Fig. 5. It is evident that larger film thickness allows for greater difference between film transmittance in oxide maxima $\Pi_{\max}$ and minima $\Pi_{\min}$ and consequently greater $B_{\max}$ value. Moreover, this increase in SEW modulation leads to stronger SEW localization at the substrate surface in case of full film oxidation at SEW maxima.

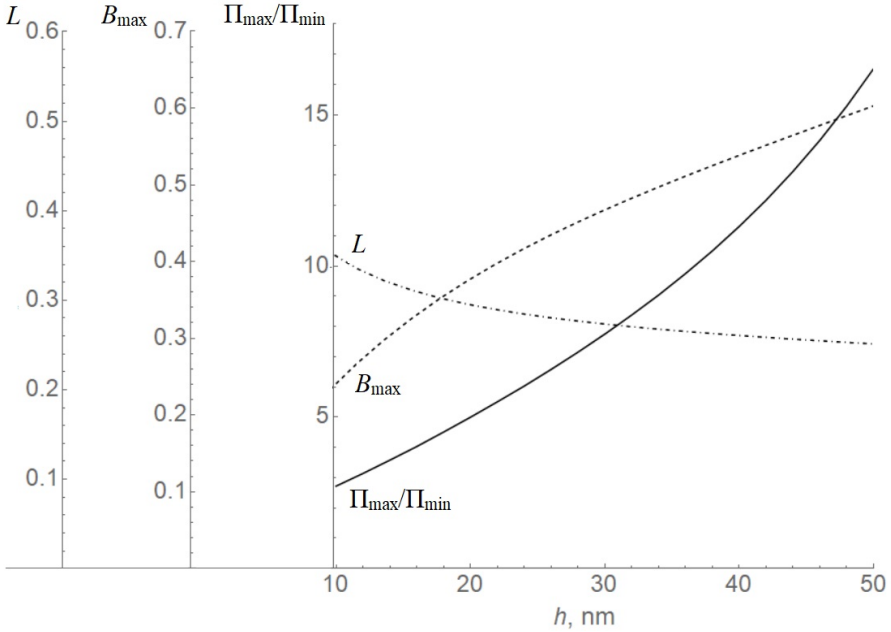

FIG. 5. Dependencies of the ratio of the fully oxidized and fully metallic film transmittance $\Pi_{\max}/\Pi_{\min}$, the maximum value of the modulation coefficient $B_{\max}$ and the penetration depth of the SEW into the substrate at $x = n\Lambda$ relative to the period of the structure $L = l/\Lambda$ for complete oxidation of the film at $x = 0$ on initial thickness of the metal film h. It is assumed that the optical characteristics of the resulting oxide correspond to rutile (values taken from [26]).

3.3. Trigonometric solution

For a more complete understanding of the regularities of the process, let us expand this analytical investigation. The values of the coordinate x and time t that describe SEW propagation in the substrate can be determined taking into account the relationship between the wave number and the period of the structure $\Lambda = 2\pi/k_s$. This situation corresponds to the real values of the χ and positive values of the right side of equation (6):

$$\cos(2\pi x/\Lambda) \cdot (1 + \tan(2\pi x/\Lambda)\tan(\omega t)) > 0. \tag{9}$$

Transforming the expression (9) we obtain the areas on the diagram (Fig. 6(a)) depending on the signs of the quantities $\cos(2\pi x/\Lambda)$, $\tan(2\pi x/\Lambda)$ and $1+\tan(2\pi x/\Lambda)\tan(\omega t)$, that correspond to the condition for the propagation of the SEW in the substrate. Solid curves in the Fig. 6(a) correspond to function $\gamma = -1/\beta$ and dashed curves correspond to function $\gamma = 2\beta/3 - 1/(3\beta)$. For each area of the graph, the black icon indicates the quadrant in which $2\pi x/\Lambda$ is located. For example, the icon with the square in the upper right corner corresponds to values $2\pi x/\Lambda \in (0; \pi/2)$. In order to obtain the characteristics of the SEW location in the actual coordinates (x, t), we transform the data from Fig. 6(a) to the coordinates $(2\pi x/\Lambda, \gamma)$ first, taking into account the distribution by quadrants, and then to the coordinates $(2\pi x/\Lambda, \omega t)$. The results are presented in Fig. 6(b). The graph shows one period in time and coordinate, which can be translated up and to the right, respectively. The lines separating the areas of SEW location in the substrate are described by the following functions:

$$\omega t = -\arctan(\cot(2\pi x/\Lambda)) \quad \text{for} \quad \cos(2\pi x/\Lambda) > 0, \tag{10}$$

$$\omega t = -\arctan\left(\frac{1}{3}\cot(2\pi x/\Lambda) - \frac{2}{3}\tan(2\pi x/\Lambda)\right) \quad \text{for} \quad \cos(2\pi x/\Lambda) < 0, \tag{11}$$

where $\alpha = 2\pi x/\Lambda$. Nonlinear functions (10–11) can be given in general form as $\omega t = \arctan[(2/3)\tan\alpha - (1/3)\cot\alpha]$, or approximated by linear functions with an error less than 0.09. Main applicable dependencies including the time durations of SEW localization in hotspots near the surface can be easily found from the relations given in the simplified system (10–14).

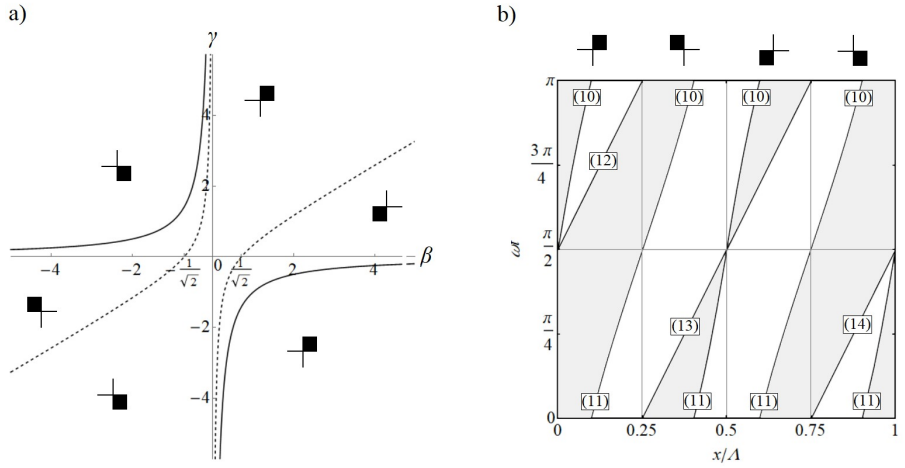

FIG. 6. (a) Areas in coordinates $\beta = \tan(2\pi x/\Lambda)$, $\gamma = \tan(\omega t)$, corresponding to the SEW location in the substrate. (b) Characteristics of the SEW location. Gray color indicates the areas of time-coordinate values where the SEW locates in the substrate, white domains indicates values at which it goes up into the air. Numbers in brackets in front of the curves correspond to the formulas in the text.

4. Conclusions

In this study, we theoretically and experimentally investigated the formation of LIPSS at optically thin films for the case of the 30, 60 and 80 nm titanium films. We show that LIPSS formation on thin metal films cannot be covered by conventional models, as the calculations predict the appearance of LSFL-I type structures with periods of about 0.998λ (1062 nm for our conditions), while our experimental results show the consistent formation of LSFL-II type structures with periods of about 0.658λ – 0.695λ (720 ± 20 nm). To address this discrepancy, we have developed a fully analytical model that describes the electric field dynamics considering the surface electromagnetic wave induced not on the air-film, but on the film-substrate interface. The main results of the study are as follows:

1. In case of an optically small film thickness (comparable or less to the depth of laser radiation penetration into the film), the conditions are created for the formation of SEW at the film–substrate interface. The thickness of the film should ensure sufficient transmission of laser radiation into the substrate, comparable in magnitude with the radiation absorbed in the film.
2. The main cause for the formation of LIPSS in the film due to the formation of SEW at the film–substrate interface is the uneven transmittance of the film due to its local oxidation.
3. The period of LIPSS formed in the film as a result of the formation of SEW at the film-substrate interface depends on the refractive index of the substrate material n_{sub} and, as follows from the experiments, is equal to λ/n_{sub}.
4. The results of calculations based on the phenomenological model showed the existence of a positive feedback between the local thickness of the oxide layer and the concentration of SEW energy within the areas of $\pm 0.1x/\lambda$ from the modulated field maxima, which makes it possible for the oxide layer to grow further despite the bleaching the Ti film during its oxidation.
5. Full spatiotemporal dynamics of SEW propagation in substrate can be described with the system of trigonometric solutions, which can be further linearized with the margin of error less than 0.09. The derived analytical system is instrumental for understanding the processes underlying the method of direct LIPSS-based nanopatterning of thin films and could help in the selection of film thicknesses for the applications in photonics.

References

[1] Feng E., Zhang C., Chang J., Han Y., Li H., Luo Q., Ma C.Q., Yip H.L., Ding L., Yang J. A 16.10 % efficiency organic solar module with ultra-narrow interconnections fabricated via nanosecond ultraviolet laser processing. *Cell Reports Physical Science*, 2024, **5** (3), 101883.

[2] Nirmal A., Kyaw A.K.K., Jianxiong W., Dev K., Sun X., Demir H.V. Light Trapping in Inverted Organic Photovoltaics with Nanoimprinted ZnO Photonic Crystals. *IEEE J. of Photovoltaics*, 2017, **7** (2), P. 545–549.

[3] Dang S., Ye H. A visible-infrared-compatible camouflage photonic crystal with heat dissipation by radiation in 5–8 μm. *Cell Reports Physical Science*, 2021, **2** (11), 100617.

[4] Bronnikov K., Terentyev V., Simonov V., Fedyaj V., Simanchuk A., Babin S.A., Lapidas V., Mitsai E., Cherepakhin A., Zhang J., Zhizhchenko A. Highly Regular Laser-Induced Periodic Surface Structures on Titanium Thin Films for Photonics and Fiber Optics. *ACS Applied Materials & Interfaces*, 2024, **16** (50), P. 70047–70056.

[5] Dostovalov A., Bronnikov K., Korolkov V., Babin S., Mitsai E., Mironenko A., Tutov M., Zhang D., Sugioka K., Maksimovic J., Katkus T. Hierarchical anti-reflective laser-induced periodic surface structures (LIPSSs) on amorphous Si films for sensing applications. *Nanoscale*, 2020, **12** (25), P. 13431–13441.

[6] Banerjee D., Akkanaboina M., Kanaka R.K., Soma V.R. Femtosecond Bessel beam induced ladder-like LIPSS on trimetallic surface for SERS-based sensing of Tetryl and PETN. *Applied Surface Science*, 2023, **616**, 156561.
[7] Pan X., Zhou L., Hu D., He W., Liu P., Yu Z., Liang X. Superior wear resistance in cast aluminum alloy via femtosecond laser induced periodic surface structures and surface hardening layer. *Applied Surface Science*, 2023, **636**, 157866.
[8] Sotelo L., Fontanot T., Vig S., Herre P., Yousefi P., Fernandes M.H., Sarau G., Leuchs G., Christiansen S. Influence of initial surface roughness on LIPSS formation and its consecutive impact on cell/bacteria attachment for TiAl6V4 surfaces. *Advanced Materials Technologies*, 2023, **8** (12), 2201802.
[9] Andreeva Y.M., Luong V.C., Lutoshina D.S., Medvedev O.S., Mikhailovskii V.Y., Moskvin M.K., Odintsova G.V., Romanov V.V., Shchedrina N.N., Veiko V.P. Laser coloration of metals in visual art and design. *Optical Materials Express*, 2019, **9** (3), P. 1310–1319.
[10] Ibrahim Q., Andreeva Y., Suvorov A., Khmelenin D., Grigoryev E., Shcherbakov A.A., Sinev D. Laser fabrication of 1D and 2D periodic sub-wavelength gratings on titanium films. *Optics & Laser Technology*, 2024, **174**, 110642.
[11] Bonse J., Gräf S. Maxwell meets Marangoni – a review of theories on laser-induced periodic surface structures. *Laser & Photonics Reviews*, 2020, **14** (10), 2000215.
[12] Öktem B., Pavlov I., Ilday S., Kalaycıoğlu H., Rybak A., Yavaş S., Erdoğan M., Ilday F.Ö. Nonlinear laser lithography for indefinitely large-area nanostructuring with femtosecond pulses. *Nature Photonics*, 2013, **7** (11), P. 897–901.
[13] Sinev D.A., Yuzhakova D.S., Moskvin M.K., Veiko V.P. Formation of the submicron oxidative LIPSS on thin titanium films during nanosecond laser recording. *Nanomaterials*, 2020, **10** (11), 2161.
[14] Belousov D.A., Bronnikov K.A., Okotrub K.A., Mikerin S.L., Korolkov V.P., Terentyev V.S., Dostovalov A.V. Thermochemical laser-induced periodic surface structures formation by femtosecond laser on Hf thin films in air and vacuum. *Materials*, 2021, **14** (21), 6714.
[15] Yang H.Z., Jiang G.D., Wang W.J., Mei X.S., Pan A.F., Zhai Z.Y. Picosecond laser fabrication of nanostructures on ITO film surface assisted by pre-deposited Au film. *Applied Physics B*, 2017, **123** (10), 251.
[16] Dostovalov A.V., Derrien T.J.-Y., Lizunov S.A., Přeučil F., Okotrub K.A., Mocek T., Korolkov V.P., Babin S.A., Bulgakova N.M. LIPSS on thin metallic films: New insights from multiplicity of laser-excited electromagnetic modes and efficiency of metal oxidation. *Applied Surface Science*, 2019, **491**, P. 650–658.
[17] Dostovalov A.V., Korolkov V.P., Okotrub K.A., Bronnikov K.A., Babin S.A. Oxide composition and period variation of thermochemical LIPSS on chromium films with different thickness. *Optics Express*, 2018, **26** (6), P. 7712–7723.
[18] Bronnikov K., Gladkikh S., Okotrub K., Simanchuk A., Zhizhchenko A., Kuchmizhak A., Dostovalov A. Regulating morphology and composition of laser-induced periodic structures on titanium films with femtosecond laser wavelength and ambient environment. *Nanomaterials*, 2022, **12** (3), 306.
[19] Badía-Majós A., Martínez E., Angurel L.A., de la Fuente G.F., Fourneau E., Marinković S., Silhanek A.V. Laser nanostructured metasurfaces in Nb superconducting thin films. *Applied Surface Science*, 2024, **649**, 159164.
[20] Xu L., Geng J., Shi L., Cui W., Qiu M. Impact of film thickness in laser-induced periodic structures on amorphous Si films. *Frontiers of Optoelectronics*, 2023, **16** (1), 16.
[21] Fraggelakis F., Lingos P., Tsibidis G.D., Cusworth E., Kay N., Fumagalli L., Kravets V.G., Grigorenko A.N., Kabashin A.V., Stratakis E. Double-Pulse Femtosecond Laser Fabrication of Highly Ordered Periodic Structures on Au Thin Films Enabling Low-Cost Plasmonic Applications. *ACS Nano*, 2025, **19** (25), P. 23258–23275.
[22] Derrien T.J.-Y., Krüger J., Bonse J. Properties of surface plasmon polaritons on lossy materials: lifetimes, periods and excitation conditions. *J. of Optics*, 2016, **18** (11), 115007.
[23] Johnson P.B., Christy R.W. Optical constants of transition metals: Ti, V, Cr, Mn, Fe, Co, Ni, and Pd. *Physical Review B*, 1974, **9** (12), P. 5056–5070.
[24] Libenson M.N. *Laser-induced optical and thermal processes in condensed matter and their mutual influence*. Nauka Publisher, St. Petersburg, 2007. 423 p. (in Russian).
[25] Malitson X.I.H. Interspecimen comparison of the refractive index of fused silica. *J. of the Optical Society of America*, 1965, **55** (10), P. 1205–1209.
[26] Devore J.R. Refractive indices of rutile and sphalerite. *J. of the Optical Society of America*, 1951, **41** (6), P. 416–419.

Submitted 1 August 2025; accepted 23 November 2025

Information about the authors:

Andrey S. Khramov – ITMO University, St. Petersburg, 197101, Russia; ORCID 0000-0002-3895-0728; askhramov@itmo.ru

Maksim D. Vasilev – ITMO University, St. Petersburg, 197101, Russia; ORCID 0009-0000-2686-290X; mdvasilev@itmo.ru

Dmitry A. Sinev – ITMO University, St. Petersburg, 197101, Russia; ORCID 0000-0002-6274-1491; sinev@itmo.ru

Elena A. Shakhno – ITMO University, St. Petersburg, 197101, Russia; ORCID 0000-0001-8005-8410; elena.shakhno@mail.ru

Conflict of interest: the authors declare no conflict of interest.